minerals

MDPI

Article

Effects of Dolomite on Mineral Compositions and Metallurgical Properties of Chromium-Bearing Vanadium–Titanium Magnetite Sinter

Songtao Yang [1,2], Weidong Tang [1,3], Mi Zhou [1,3,*], Tao Jiang [1,3], Xiangxin Xue [1,3,*] and Weijun Zhang [1]

[1] School of Metallurgy, Northeastern University, Shenyang 110819, China; yangsongtao1984@163.com (S.Y.); twdking@163.com (W.T.); jtyz@163.com (T.J.); zhangwj@smm.neu.edu.cn (W.Z.)
[2] School of Materials and Metallurgy, University of Science and Technology Liaoning, Anshan 114051, China
[3] Key Laboratory of Liaoning Province for Recycling Science of Metallurgical Resources, Shenyang 110819, China
* Correspondence: zhoum@mail.neu.edu.cn (M.Z.); xuexx@mail.neu.edu.cn (X.X.)

Received: 22 July 2017; Accepted: 30 October 2017; Published: 2 November 2017

Abstract: Chengde chromium-bearing vanadium–titanium magnetite (CCVTM) has been used as an important mineral resource in sinter making. The MgO content of this sinter can be enhanced by adding dolomite, which improved operation of the blast furnace. The effects of MgO in the form of dolomite on metallurgical properties, microstructure and mineral compositions of CCVTM sinter were studied by a sinter pot test, X-Ray Diffraction (XRD), Scanning Electron Microscope (SEM), and mineral phase microanalysis. The results were as follows: The flame front speed and sinter coefficient decreased with an increase in MgO content from 2.66 to 3.86% by adding dolomite. With an increase in MgO content from 2.66 to 3.86%, the flame front speed, sintering utilization factor, and the value of RI decreased, while RDI and the softening–melting properties improved. In addition, the value of sinter strength (TI) reached a maximum value at MgO = 3.56%. In addition, an increase in the abundance of magnetite, magnesium ferrite, and silicate phase, as well as a decrease in hematite, was found with an increase in MgO content. We concluded that the most appropriate MgO content in the sinter is 3.56%.

Keywords: vanadium–titanium magnetite; sinter; mineralogical phases; metallurgical properties; MgO

1. Introduction

The development of mineral separation techniques has allowed the utilization of Chengde chromium-bearing vanadium–titanium magnetite (CCVTM). Chromium and vanadium resources have been extracted from CCVTM [1–7]. The viscosity and the TiO_2 content of the slag are high in the blast furnace (BF) iron-making process, due to the high TiO_2 content in the CCVTM. The slag experiences a decreased ability for desulfurization, and it is difficult to separate the slag from the iron [8–13].

MgO has a substantial influence on the BF iron-making process. This was reflected in the positive influence that the MgO content had on the liquidity, the stability, and the desulfurization ability of the slag and the metallurgical properties of sinter. The liquidity, desulfurization, and dealkalization capacities of the slag could be improved by using a high MgO content of sinter in the BF. The techno-economic indexes of BF can also enhanced when the properties of slag are enhanced [14–16]. However, the production requirements of the BF cannot be met with the original low MgO content of the CCVTM. A cheap dolomite was used to increase the MgO content in the CCVTM sinter; however, the quality of the CCVTM sinter was affected by the dolomite.

Yu et al. [17,18] found that increasing the MgO could decrease the glass phase content in the sintered matrix. This improves the high temperature reducibility and the softening–melting properties. The increased MgO decreases the sinter strength in the high-silicate sinter. Zhao et al. [19–22] explored the question of whether the increases in the bonding phase content, the refinement of grains, the improvements of compositions, the structures of sinter, and the enhanced sinter strength were related to the increase in MgO content in the low basicity sinter. The effect and mechanism of MgO on the sinter quality were varied and controversial, due to the lack of relevant research. This was especially controversial within the complicated mineral compositions of the CCVTM.

In this paper, an iron ore raw material was used for the CCVTM. The MgO content was adjusted by adding dolomite. The effect of the MgO content on the CCVTM sinter was explored with the sinter pot test. The flame front speed and the coefficients were calculated. The mineral compositions and the mineral phase microstructures of the sinter over various MgO concentrations were studied. The metallurgical properties of the CCVTM sinter over various MgO concentrations were tested. The mechanism that the MgO has on the mineral compositions and the sinter quality were revealed. Finally, the appropriate MgO content was analyzed with a comprehensively weighted grading method.

2. Materials and Methods

2.1. Materials

The raw materials used in the sinter pot test, including CCVTM, ordinary iron ore, dolomite, ash, vanadium extraction tailings, were purchased from the Jianlong Steel Company (Chengde, China). The CCVTM was a blend of CCVTM mixed by Daban (DB), Henwei (HW), Yuantong (YT), and Jianlong (JL) ores produced in the Chengde areas, Hebei Province, China. The chemical compositions of raw materials are shown in Table 1. The analysis of the industrial coke is shown in Table 2. The XRD pattern and the basic characteristics of the CCVTM are shown in Figure 1 and Table 3.

The CCVTM had a high total iron content (TFe), while the MgO, TiO_2, and Al_2O_3 content levels were lower than Panzhihua VTM's [8,9]. The Cr_2O_3 content of the CCVTM was 0.12%. The CCVTM was divided into low chromium vanadium and titanium magnetite. The Fe element was in the form of magnetite, ulvospinel, and ilmenite. The Ti element primarily formed titanomagnetite and ilmenite. Vanadium was mainly associated with magnetite. The Fe_2O_3 in magnetite was replaced by V_2O_3 to become $FeO{\cdot}V_2O_3$. Chromium was generated as ishkulite, with an isomorphic replacement in magnetite. The CCVTM had a high assimilation ability with an assimilation temperature of 1513 K, a poor liquidity index of 0.04, a medium bonding phase strength of 4310 N, and a large crystal stock strength of 7506 N.

Table 1. Chemical compositions of the raw materials (mass %).

Item	TFe	SiO_2	CaO	MgO	Al_2O_3	TiO_2	V_2O_5	Cr_2O_3
CCVTM (DB)	63.08	4.41	4.73	1.52	1.44	1.98	0.42	0.03
CCVTM (YT)	63.81	3.84	0.77	0.74	1.95	3.15	0.59	0.04
CCVTM(HW)	63.62	3.20	1.28	1.12	1.82	2.61	0.53	0.11
CCVTM (JL)	63.52	4.20	1.69	1.76	1.23	1.45	0.37	0.12
CCVTM (Mixed)	63.50	3.96	1.46	1.25	1.57	2.18	0.50	0.08
Iron ore A	56.06	5.57	0.06	0.15	5.63	0.21	-	-
Iron ore B	51.71	6.57	0.21	0.15	8.48	0.33	-	-
Iron ore C	65.55	3.04	0.46	3.50	0.65	0.09	-	-
Gas ash	33.28	7.26	5.65	1.98	4.55	1.32	0.25	-
Vanadium extraction tailings	30.68	16.97	2.44	2.82	1.53	9.81	1.22	-
Dolomite	-	2.47	44.26	31.67	-	-	-	-
Quicklime	-	2.52	83.07	3.50	-	-	-	-

Table 2. Proximate analysis of the coke breeze and the ash composition (wt %).

Fixed Carbon	Total Sulfur	Volatile	Ash (14.00)						Σ
			FeO	CaO	SiO_2	MgO	Al_2O_3	Others	
84.00	0.50	1.50	0.14	0.48	7.50	0.15	2.72	2.89	100.00

Table 3. The basic characteristics of the Chengde chromium-bearing vanadium–titanium magnetite (CCVTM).

Raw Material	Assimilation Temperature/K	Liquidity Index (R = 1.9; T = 1523 K)	Strength of Binding Phase/N (R = 1.9; T = 1553 K)	Crystal Stock Strength/N (T = 1553 K)
CCVTM	1513	0.04	4310	7506

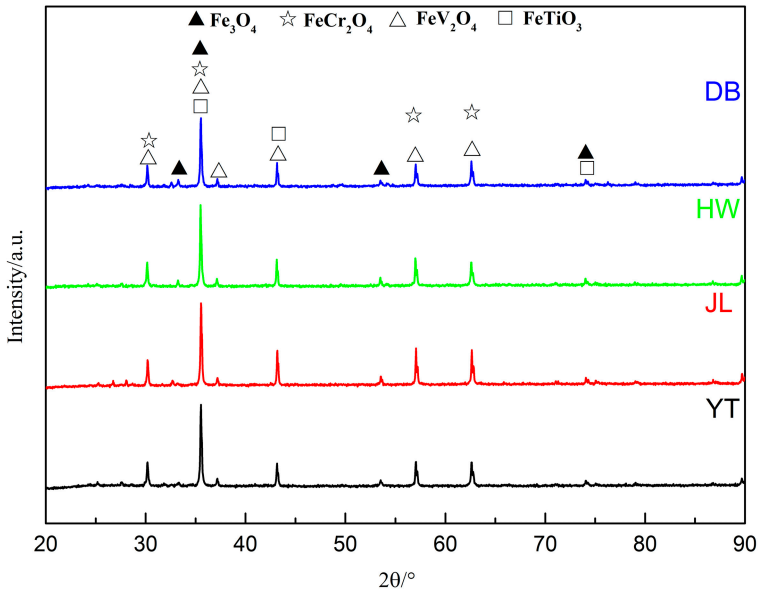

Figure 1. XRD patterns of the CCVTM (DB—Daban, HW—Henwei, JL—Jianlong, and YT—Yuantong).

2.2. Sinter Pot Test

The binary basicity was adjusted to 1.9 by quicklime with a fixed carbon content of 3.2%, in accordance to the practical situations provided by the Chengde Jianlong Steel Company. The return fine conditions were the same as the practical situations. The effect on the CCVTM sintering process and the quantity used were studied with various MgO concentrations, ranging from 2.66 to 3.86%. The raw materials were uniformly mixed and distributed. The detailed experimental scheme is shown in Table 4.

Table 4. Experimental scheme of the sinter materials (mass %).

Item	ω(MgO)	CCVTM (Mixed)	Iron Ore A	Iron Ore B	Iron Ore C	Return Fine	Ash	Vanadium Extraction Tailings	Dolomite
1	2.66	50	5	5	8	28	1	2	1
2	2.96	49	5	5	8	28	1	2	2
3	3.26	48	5	5	8	28	1	2	3
4	3.56	47	5	5	8	28	1	2	4
5	3.86	46	5	5	8	28	1	2	5

The experimental procedure of the sinter pot test that contains burdening, mixture, granulation, ignition, sintering, cooling, and crushing [2]. The operation parameters of the sinter pot test are shown in Table 5. The granulated mixture was placed in the sinter pot and ignited for 2 min at 1373 K. The sinter was cooled in air for 10 min and poured out of the sinter pot for crushing. The

crushed sinter was dropped from 2 m, 3 times, and sieved into 5 different particle sizes: <5 mm, 5–10 mm, 10–25 mm, 25–40 mm, and >40 mm.

Table 5. Parameters of the sintering test.

Item	Parameter	Item	Parameter
Bed Height	700 mm	Sintering pot diameter:	320 mm
Ignition Suction	6.0 kPa	Exhausting suction:	10.0 kPa
Ignition Temperature	1373 K	Ignition time:	2 min
Height of Hearth Layer	20 mm	Moisture:	7.5 ± 0.3%
Granulation Time	10 min		

2.3. Metallurgical Properties Test and Mineral Phase Analysis

The metallurgical properties of Sinter, including the tumble index (TI), the low-temperature reduction disintegration index (RDI), and the reducibility index (RI), were calculated in accordance with the ISO-3271, the ISO-4696, and the ISO-7215. The mineral phases of samples were quantified via XRD analysis (MPD/PW3040, Panalytical, Almelo, The Netherlands) using Cu Kα radiation (λ = 0.15406 nm) at an operating voltage of 40 kV and a current of 50 mA. The diffraction angle (2θ) was scanned from 10° to 90°.

The sinter was not a pure crystalline substance and does not have a fixed melting point, as it remains within the zone of softening–melting. As such, there is no unified standard method to determine the softening properties. The following method was used to determine the softening properties. The schematic diagram of the experimental apparatus is shown in Figure 2.

The three-stage heating process of the softening melting test was performed as follows. In the first stage, the temperature was increased from room temperature to 1173 K, at a heating rate of 10 K/min, in an N_2 flow at a rate of 3 L/min. During the second stage, the temperature was increased from 1173 to 1293 K, at a heating rate of 3 K/min, in a mixed gas flow with 9 L/min N_2, 3.9 L/min CO, and 2.1 L/min CO_2. In the third stage, the temperature was increased from 1293 to 1823 K, at a heating rate of 5 K/min, in a mixed gas flow with 10.5 L/min N_2 and 4.5 L/min CO. The softening start temperature ($T_{10\%}$) was defined when the height of the sample shrank by 10%. The softening ending temperature ($T_{40\%}$) was defined when the height of the sample shrank by 40%. The softening temperature range was from $T_{10\%}$ to $T_{40\%}$. The particle sizes of experimental sinter ranged from 2.5 mm to 3.2 mm. The loading was 1 kg/cm^2. The stock column height of the sample was 40 mm.

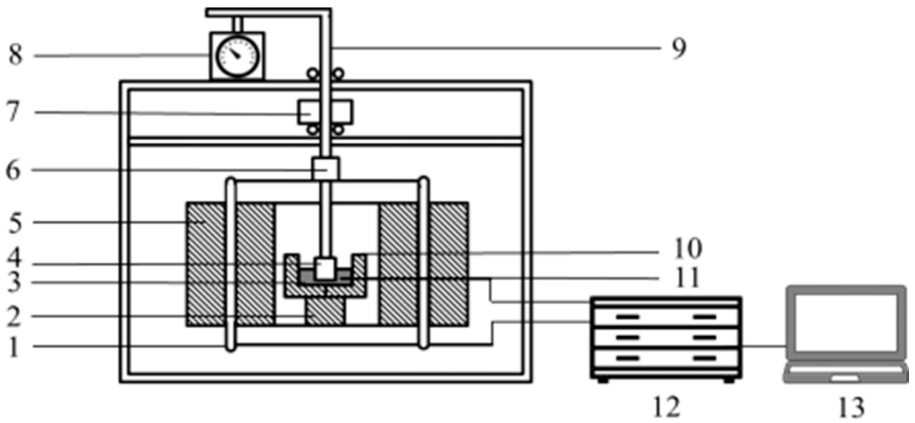

Figure 2. Schematic diagram of the softening properties experimental apparatus. 1—Si-C heater; 2—shell; 3—Al_2O_3 pedestal; 4—sample; 5—Si-C bar; 6—fastening screws; 7—load; 8—meter; 9—steel bar; 10—bracket; 11—graphite crucible; 12—thermocouple; 13—temperature program controller.

Some representative samples in the upper layer, the middle layer, and the bottom layer were selected in each experiment. The sinter samples that were obtained from each experiment were cut

into a block 3 cm by 2 cm. The block was then mounted onto an epoxy resin, which was polished with coarse sand paper (with a grit between 100 and 1500 mesh). These samples were then polished in a polisher, cleaned with water, and dried in an oven at 378 K for 4 hours. The samples were observed and analyzed with a metallurgical microscope (DM1750M, Leica, Wetzlar, Germany). The mineral phase microscope analysis data provided the average statistical area of each mineral and the total observational scope area. These measurements were obtained with an image analyzer (Q500, Leica, Cambridge, UK). The sinter samples were analyzed with a scanning electron microscope (JEOL S-3400N, Hitach, Kyoto, Japan).

3. Results and Discussion

3.1. Operation Parameters of Sintering Process

Figure 3 shows the change that occurred during the operation parameters of the sintering process of the CCVTM with various MgO concentrations. The flame front speed decreased from 15.22 to 14.58 mm/min when the MgO content increased. The peak temperature of the flue gas decreased from 481 to 462 K. It is difficult to assimilate magnesium minerals assimilation in the highly fluxed composition. MgO acted as a refractory phase and the magnesium remained either in the relicts or in the reaction zones. The MgO formed a melted complex with SiO_2 at temperatures >1623 K and with Fe_2O_3 at temperatures >1873 K. The addition of the MgO increased the liquid temperature of the melt [15], especially when the assimilation temperature of the CCVTM was low (1523 K). This resulted in a decreased flame front speed. The decomposition process of dolomite required extra energy, so the peak temperature of flue gas decreased at a constant rate. The productivity of sinter changed slightly from 1.17 to 1.14 t/m^2·h.

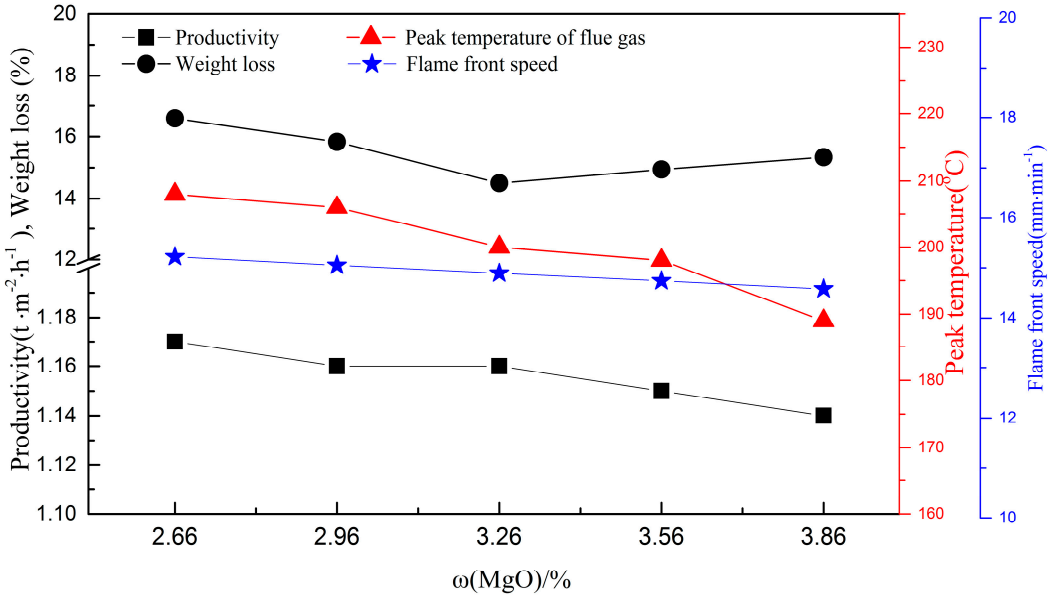

Figure 3. Effect of ω(MgO) on the CCVTM sintering process.

Figure 4 shows the particle size distributions of the sinter with various MgO concentrations. The large particles and the small particles increased when the MgO content increased. The medium-sized particles decreased. The increased viscosity of the liquid phase, the poor liquidity of the liquid phase, and the non-uniform distribution of the particle sizes were caused by the increase in generation temperature of the liquid phase with an increase in MgO content in the sintering process for a high melting point of MgO.

The fraction of the sinter particles that has a diameter less than 5 mm did not change when the MgO content increased. When there were sufficient crystals in the sinter phases, the complete development of the mineral structures and the productivity of the sinter were a result of the decreased inflame front speed, the increased sintering time, and the high temperature insulation

time. This occurred when the MgO content increased. The quantity of the liquid phase decreased when the MgO content increased at the same rate. The insufficient liquid phase of the CCVTM sinter caused the productivity of the sinter to decrease when the MgO content increased. The slight change in the sinter productivity was caused by multiple factors.

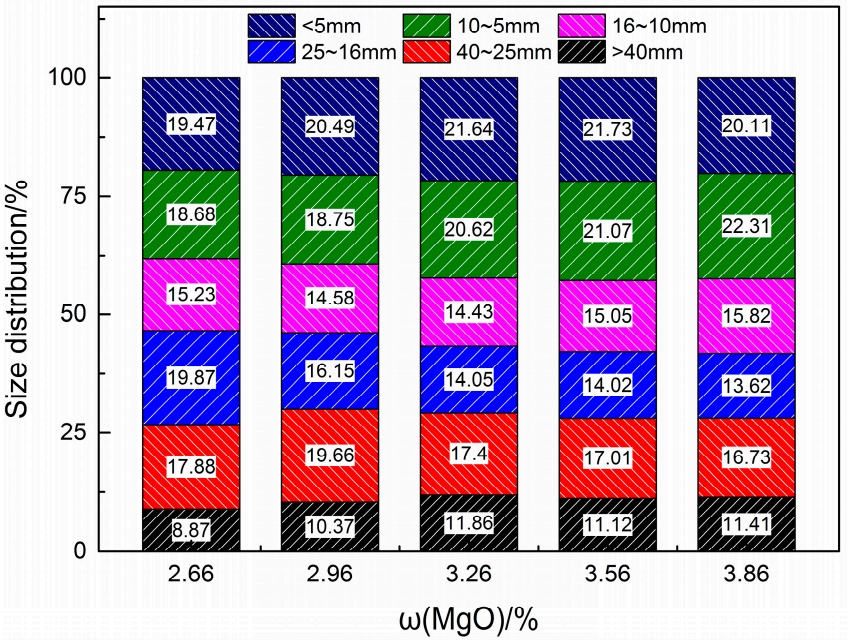

Figure 4. Particle size the distribution of CCVTM sinter with various MgO concentrations.

3.2. Mineral Composition and Microstructure

Figure 5 shows the XRD patterns of the CCVTM sinter with various MgO concentrations. The XRD patterns showed that the main mineral phases contained magnetite, hematite, perovskite, calcium ferrite, silicate, ilmenite, and some magnesium ferrite. The diverse mineral compositions of the CCVTM sinter were caused by the sintering temperature and the MgO content.

Figure 6 shows the mineral compositions of the CCVTM sinter. Magnetite, magnesium ferrite, and silicate phases increased. The hematite and glass phases decreased. The perovskite and the calcium ferrite phases changed slightly when the MgO content increased.

Figure 7 shows the microstructures of the CCVTM sinter with the various MgO concentrations ranging from 2.66 to 3.86%. The analysis of Figures 6 and 7 were combined to show that the mineral structure of the CCVTM sinter transformed from the melting state to the interconnection of the magnetite when the MgO content increased. Subsequently, the distribution of the mineral phases became disordered. Our previous research [4,5,23–25] found that, when the MgO content was 2.66%, a large number of secondary skeleton hematites were produced. The distribution of the mineral structures were non-uniform and the partial phases were in a slightly over-molten state, as shown in Figure 7a. Figure 7b shows a small amount of secondary skeleton hematite present in the sinter phases, while some perovskite was distributed in the silicate. When the MgO content was 3.86%, the secondary skeleton hematite was not observed in the sinter phases and the distributions of the mineral phase structure were more uniform than in the low MgO content. Figure 7e shows the mineral phases that contained the large grain magnetite. The generation of magnesium ferrite increased, due to the decrease in the hematite and the increase in the magnetite when the MgO content increased.

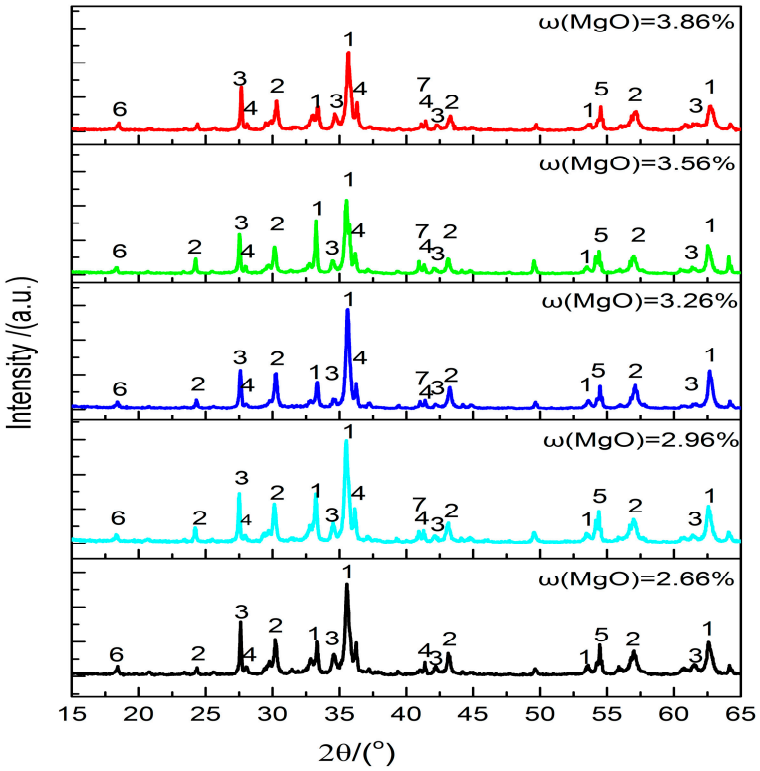

Figure 5. XRD pattern of the CCVTM sinter with various MgO concentrations: 1—Magnetite; 2—Hematite; 3—Calcium ferrite; 4—Perovskite; 5—Silicate; 6—Ilmenite; 7—Magnesium ferrite.

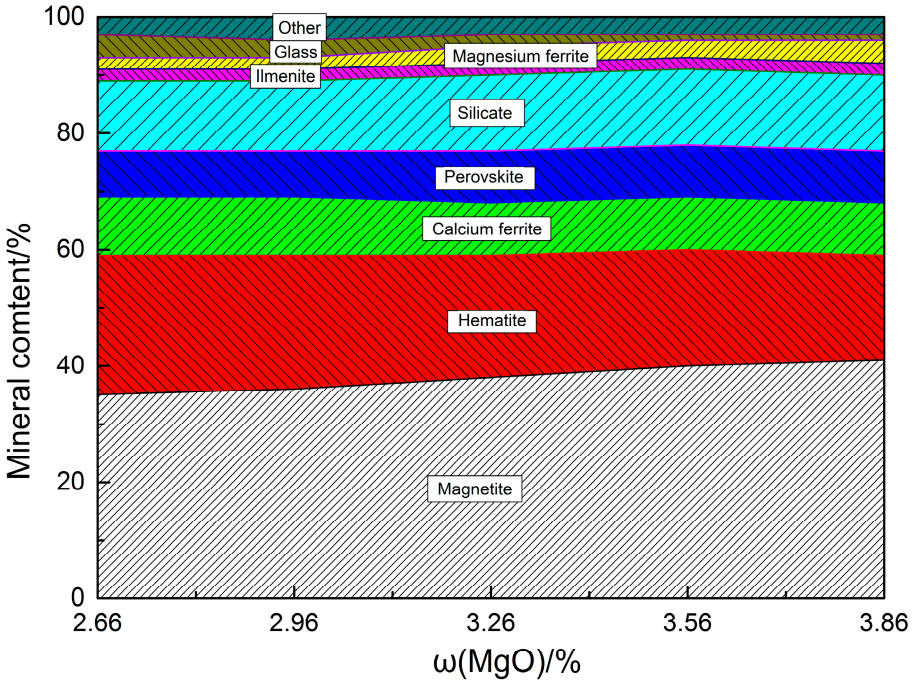

Figure 6. Mineral compositions of the CCVTM sinter with various MgO concentrations.

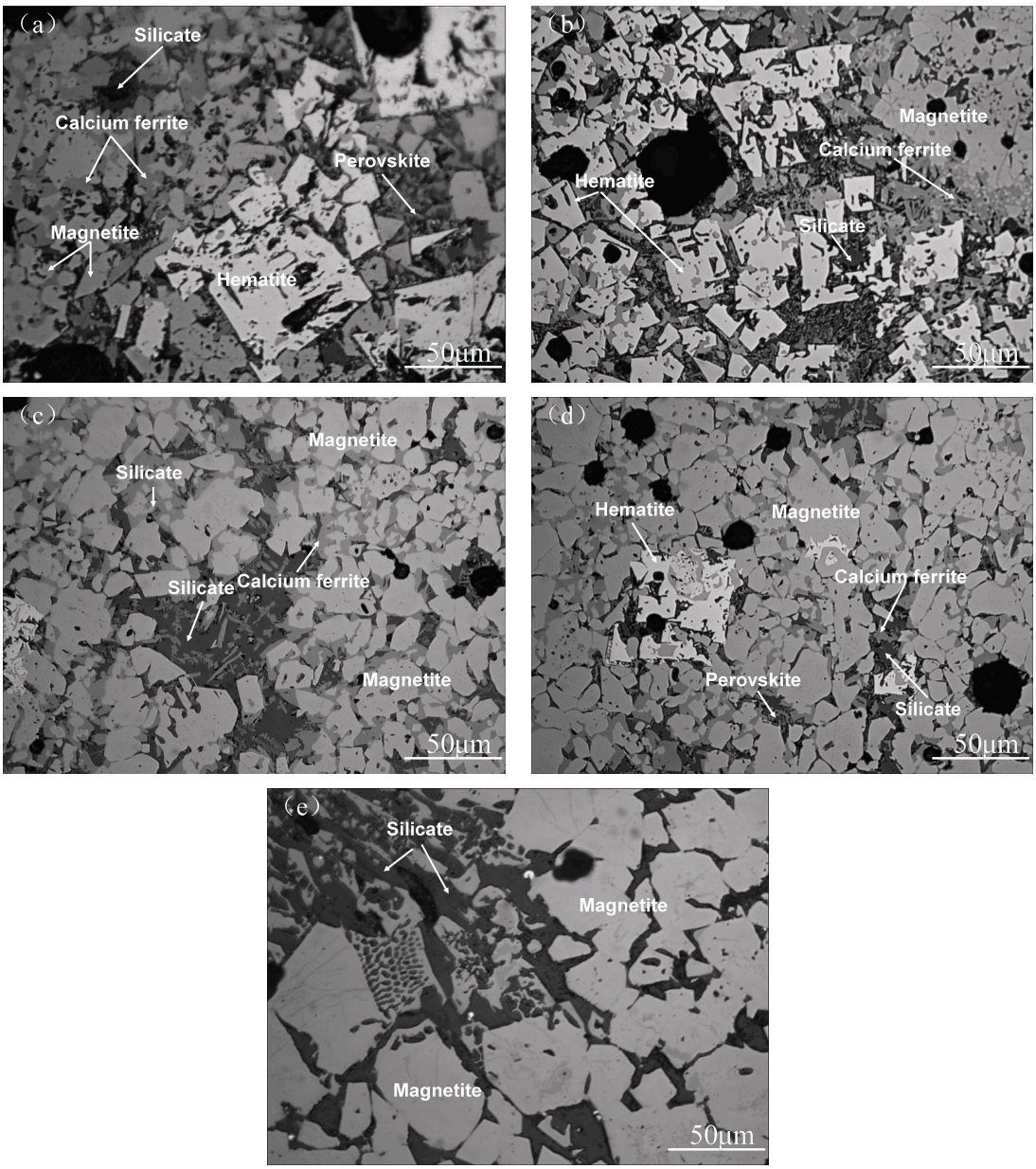

Figure 7. Microstructure of the sinter with various MgO concentrations: (**a**) ω(MgO) = 2.66%; (**b**) ω(MgO) = 2.96%; (**c**) ω(MgO) = 3.26%; (**d**) ω(MgO) = 3.56%; (**e**) ω(MgO) = 3.86%.

Figures 8 and 9 show the main existing state of the magnesium ferrite in the sinter. The magnesium ferrite phase was combined with other phases or crystalized into a spheroidal crystal phase. The majority of the Mg elements were distributed as magnesium ions in the CCVTM sinter phases. The Fe^{2+} and the Mg^{2+} has similar ionic radii (Fe^{2+}: 0.83 and Mg^{2+}: 0.78) and lattice coefficients (Fe^{2+}: 2.10 and Mg^{2+}: 2.12). This meant that Fe^{2+} could be replaced by Mg^{2+} during the sintering process. Mg^{2+} also existed as an isomorphic formation in the sinter phases. This generated multi-elemental phases, including Ca, Mg, Fe, and Si elements. Figure 10 shows the distribution of the magnesium ions in the CCVTM sinter. The formation of the magnesium that contained magnetite was (Fe, Mg) O·Fe_2O. The Mg^{2+} content increased when the dolomite was added. Fe^{2+} and Ca^{2+} were replaced with Mg^{2+}, which existed in the crystal vacancies of olivine and pyroxene. The defect degrees of the sinter phases decreased, the structure of the sinter was more stable and it was more difficult to oxidize the magnetite to regenerated the hematite. The quantities of titanomagnetite, forsterite, and pyroxene increased when the MgO content was increased by adding dolomite.

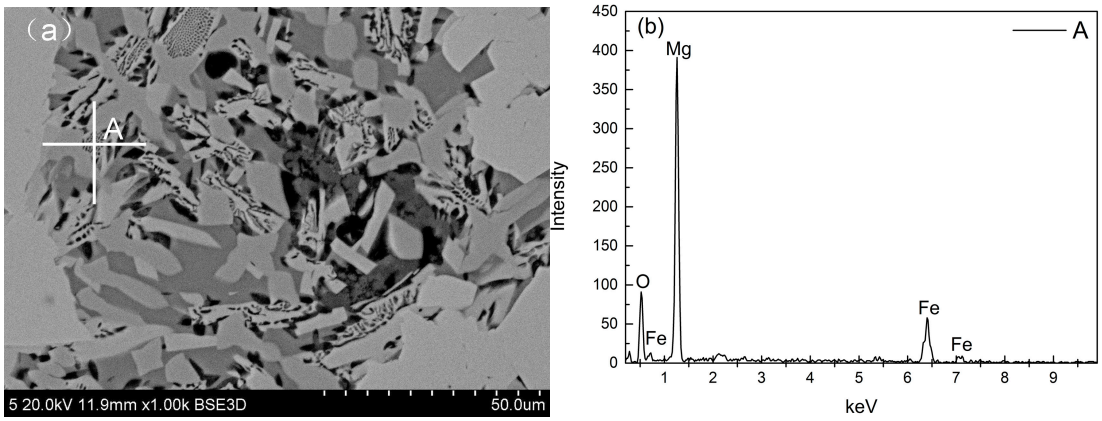

Figure 8. Magnesium ferrite and calcium ferrite bonding phases in the sinter (ω(MgO) = 3.56%): (**a**) SEM micrographs; (**b**) EDS of point A.

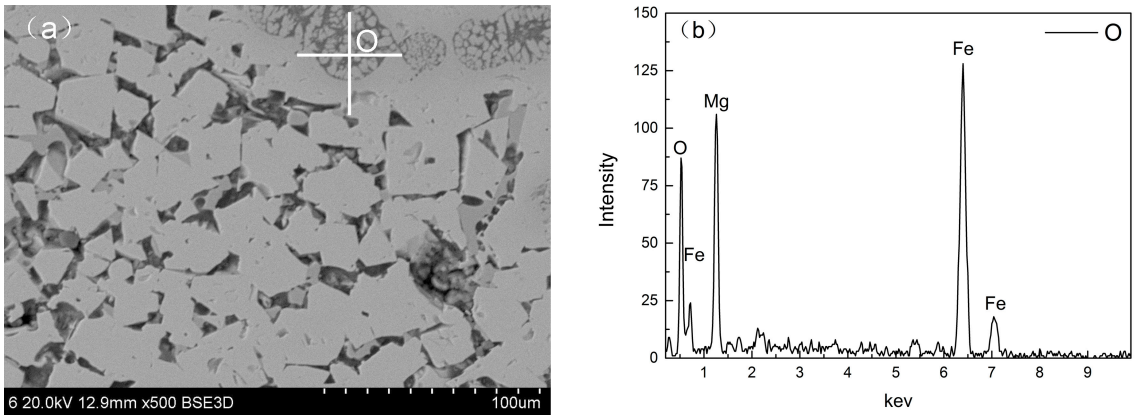

Figure 9. Spheroidal crystal of the magnesium ferrite (ω(MgO) = 3.86%): (**a**) SEM micrographs; (**b**) EDS of point O.

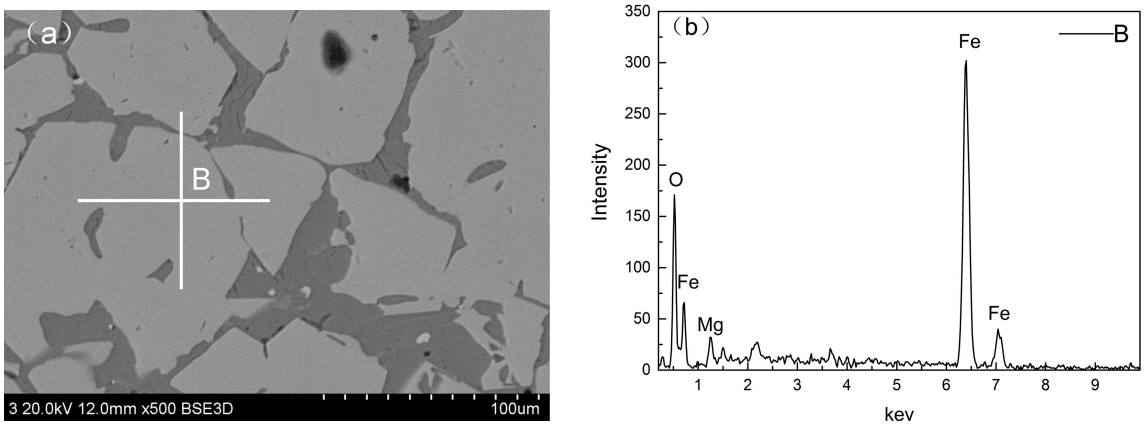

Figure 10. SEM photo of magnetite containing magnesium: (**a**) SEM micrographs; (**b**) EDS of point B.

3.3. The Effects of Metallurgical Properties

Figure 11 shows the main metallurgical properties of sinter. The TI of the sinter increased from 59.23 to 62.95%, before decreasing to 62.36% with 3.86% MgO.

The MgO was provided in the form of $CaMg(CO_3)_2$ in dolomite. The decomposition reactions of dolomite were as follows:

$$CaMg(CO_3)_2 = MgO + CaCO_3 + CO_2\ (g) \quad (1)$$

$$CaCO_3 = CaO + CO_2\ (g). \quad (2)$$

Part of the energy was consumed during the sintering process for the decomposition reactions of dolomite. The energy consumed during the decomposition reactions increased along with the MgO content. The energy requirements increased, the flame front speed, and the temperature decreased at the same fixed carbon content. The CaO-MgO-FeO-Fe_2O_3-SiO_2 phase diagram showed that the sinter strength was improved, because some magnesium that contained minerals had a high melting pointing and high strength. These included forsterite, monticellite, manganolite, and akermanite, with melting points of 2163 K, 1727 K, 1843 K, and 1727 K [26,27]. The quantities of the liquid phases could have decreased because of the decreased sintering temperature.

The phases in the CCVTM sinter, including calcium ferrite, silicate, and glass phases, played an important bonding effect for the sinter. In CCVTM sinter, due to the content of calcium ferrite is lower than that in ordinary sinter, the bonding effects of silicate and glass phases are more important. When the MgO content increased, there was an increase in the Mg-bearing silicate phases and a decrease in the glass phases were formed. The TI increased when the Mg-bearing silicate phases increased and the glass phases decreased. This was because the strength of silicate was higher than the glass phase. Meanwhile, TI increased due to stabilization of crystal bonding phases for more sintering time with the increase in MgO.

An increase in the MgO content could make the liquid phase decrease (including silicate and calcium ferrite). The pores in the sinter could be increased when the sintering was conducted in a constant coke ratio. The MgO content made the magnetite more stable and decreased the content of hematite. The decreased hematite content inhibited the generation of calcium ferrite.

The MgO obtained a proper content. A high MgO content was harmful to the improvement of the sinter strength. The TI initially increased and then decreased.

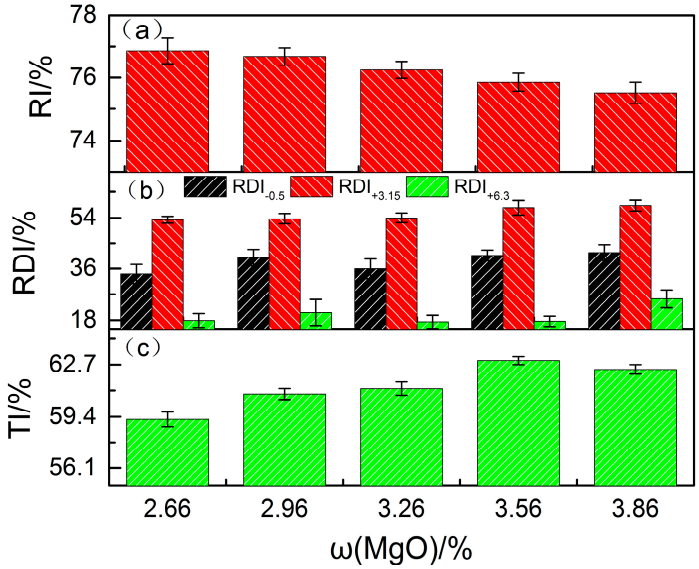

Figure 11. Metallurgical properties of the sinter with various MgO concentrations: (**a**) RI—reducibility index; (**b**) RDI—reduction disintegration index; (**c**) TI—tumble index.

The RDI increased along with the increased MgO content. The fundamental points of low temperature reduction disintegration occurred when the reduction in the regeneration of hematite ranged from 723 to 773 K. The phase transformation occurred from α-Fe_2O_3 to Fe_3O_4, when disintegration was caused by volume expansion [28–30]. The reduction disintegration improved and the hematite decreased when the hard-reduced magnetite formed a solid solution with the MgO. The crystallization ability of the silicate melt was enhanced by the MgO and the glass phase content decreased. The precipitated forsterite and the pyroxene phases were the framework used to enhance the resistance against various stresses and crack growth. The low temperature reduction disintegration of the sinter improved. The RI decreased when the MgO content increased, due to the increase of magnetite and the MgO-bearing materials with a lower reduction index.

Figure 12 shows the change that occurred in the softening–melting properties of CCVTM sinter with various MgO concentrations. $T_{10\%}$ and $T_{40\%}$ increased, due to the precipitation of the high melting point phases (magnesiomagnetite and monticellite) when the MgO content increased. The softening interval ($T_{40\%} - T_{10\%}$) narrowed, meaning that that the BF gas flow and the utilization efficiency increased, and the operation of the BF was stable. The increased MgO improved the softening–melting properties in the smelting of the CCVTM sinter.

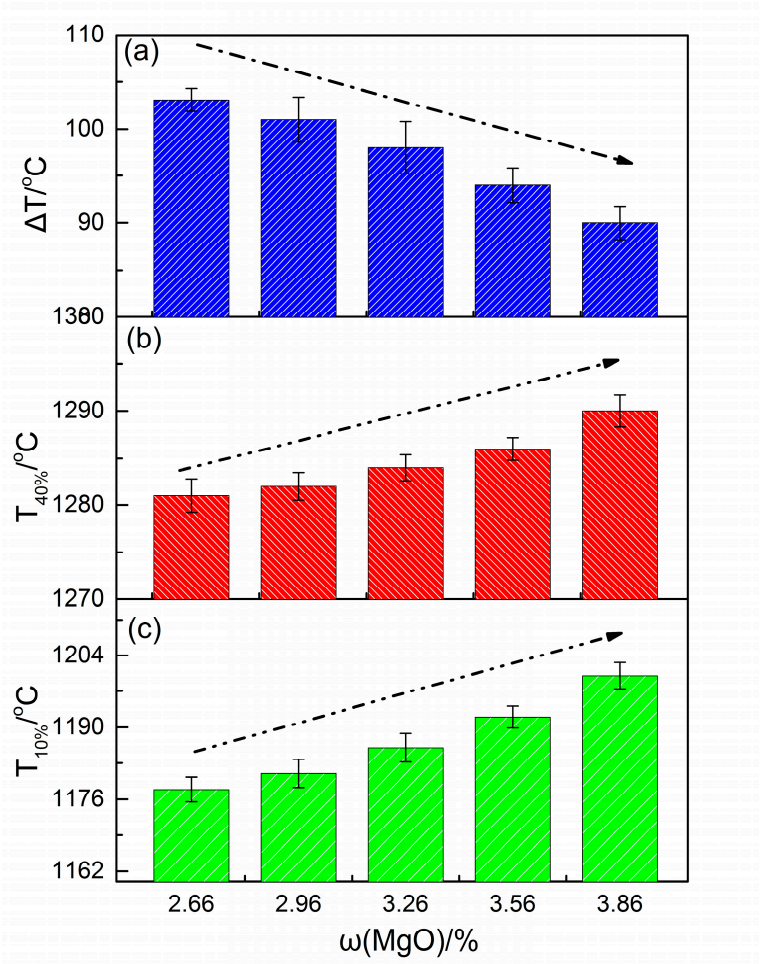

Figure 12. Softening–melting properties of the CCVTM sinter with various MgO concentrations: (**a**) T10%; (**b**) T40%; (**c**) softening interval.

3.4. Comprehensive Index

The quality and the quantity of the CCVTM sinter could be enhanced by an appropriate MgO content. The Delphi Method was used to evaluate the CCVTM sinter. This method was used to confirm the subjective weights of each sinter index. The objective weights of each sinter index were determined by the entropy evaluation method. The appropriate MgO content of the CCVTM sinter was calculated through the compound weight method, which was objective, true, and effective.

The calculation process via the compound weight method is detailed below.

The parameters of the sinter indexes are as follows: evaluation matrix = X, standard matrix = Z, subjective weight = α, objective weight = β, and comprehensive weight = w.

The evaluation matrix X was standardized to eliminate the commensurability of each index in order to unify the trend for each index. The standard matrix Z was obtained from the standardization of evaluation matrix X.

The non-commensurability among the various indexes (productivity, TI, RDI, and RI) was eliminated in order to unify the trend demands and to obtain the evaluation of matrix X = (x_{ij}).

$$X_{ij}\begin{Bmatrix}1.17 & 59.23 & 53.35 & 76.86\\ 1.16 & 60.83 & 53.7 & 76.68\\ 1.16 & 61.17 & 53.97 & 76.25\\ 1.15 & 62.96 & 57.51 & 75.85\\ 1.14 & 62.39 & 58.24 & 75.51\end{Bmatrix} \quad (3)$$

The unification of the quantitative grade of the indexes was used to standardize the results and dimension X was used to obtain the final evaluation matrix Z.

$$Z_{ij} = 100 \times (y_{ij} - y_{ij\min}/(y_{ij\max} - y_{ij\min}),\ i = 1, 2, \ldots, n;\ j = 1, 2, \ldots, m.$$

where

$$y_{ij\min} = \min\{y_{ij} \mid i = 1, 2, \ldots, n\},\ y_{ij\max} = \max\{y_{ij} \mid i = 1, 2, \ldots, n\}.$$

The values of the productivity (TI, RDI, and RI) were considered better the larger they were, so the final evaluation value should also be larger. The standardized evaluation matrix was $Z = (z_{ij})$ nm.

$$Z_{ij}\begin{Bmatrix}0.37 & 0.00 & 0.00 & 0.37\\ 0.25 & 0.15 & 0.03 & 0.32\\ 0.25 & 0.19 & 0.06 & 0.21\\ 0.12 & 0.36 & 0.42 & 0.09\\ 0.00 & 0.30 & 0.49 & 0.00\end{Bmatrix} \quad (4)$$

The weight of each sinter index was defined as a subjective weight (α):

$$\alpha = (\alpha_1, \alpha_2 \ldots \alpha_m)^T. \quad (1)$$

where

$$\sum_{j=1}^{m} \alpha_j = 1,\ \alpha_j \geq 0\ (j = 1, 2, \ldots, m).$$

The subjective weights of sinter indexes (sinter utilization factor, TI, RDI, and RI) were obtained using the Delphi Method. The weight coefficients of the sinter indexes (sinter utilization factor, RI, RDI, and TI) were confirmed by the Chengde Jianlong Steel Company (Chengde, China). The weight of sinter indexes included the sinter utilization factor = 0.1, TI = 0.3, RDI = 0.5, and RI = 0.1. The subjective weight α was defined as follows:

$$\alpha = [0.1, 0.3, 0.5, 0.1]^T. \quad (6)$$

The objective weights of the sinter index were determined by the entropy evaluation method. The objective weights matrix (β) was defined as follows:

$$\beta = [0.19, 0.19, 0.40, 0.22]^T. \quad (7)$$

The comprehensive weight of each sinter index was obtained and the matrix was defined as w. When the inclination coefficient was 0.5, the comprehensive evaluation w was calculated as follows:

$$w = \sum_{j=1}^{m} z_{ij}\alpha_j = 1 \quad i = 1, 2, \ldots, n. \quad (8)$$

The calculated values are shown below:

$$w = [0.15, 0.24, 0.55, 0.26]^T. \quad (9)$$

Figure 13 shows the comprehensive evaluation results of the CCVTM sinter with various MgO concentrations. The best evaluation result of the CCVTM sinter was 3.56% MgO with an MgO content of 2.66–3.86%.

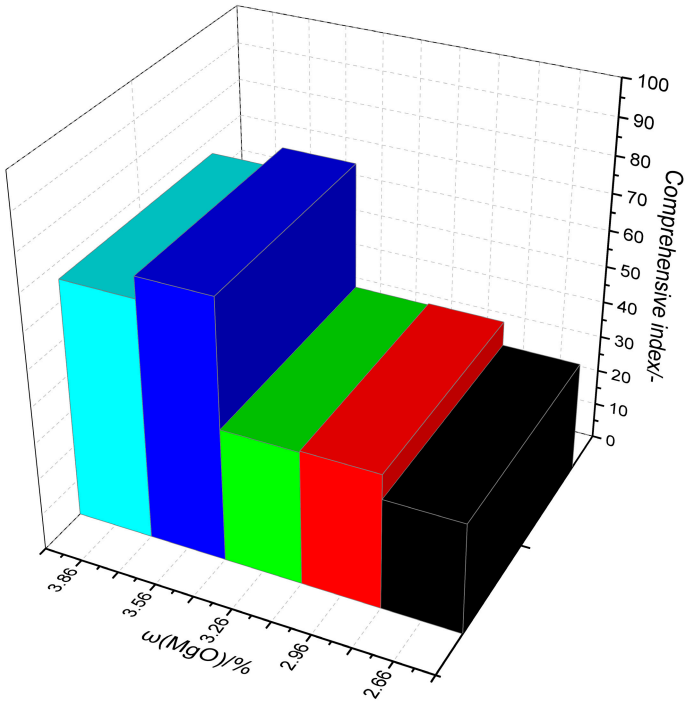

Figure 13. Comprehensive evaluation index of the CCVTM sinter with various MgO concentrations.

4. Conclusions

The results of this study led to the following conclusions:

- When the MgO content was increased from 2.66 to 3.86%, the flame front speed, the sintering utilization factor, and the value of RI decreased. The RDI and the softening–melting properties were improved. The value of the sinter strength obtained the max value at MgO = 3.56%.
- The mineral compositions of the CCVTM sinter were only slightly different when the MgO content was varied. The ferrous minerals primarily contained magnetite and hematite. The bonding phases primarily contained calcium ferrite, silicate, and glass phases. When the MgO content increased, the magnetite, the magnesium ferrite, and the silicate phases increased, while the hematite and glass phases decreased.
- The comprehensive evaluation results first increased and then decreased when the MgO content increased. The appropriate MgO content was 3.56%.

Acknowledgments: This research was financially supported by the Programs of the National Natural Science Foundation of China (Nos. 51604065, 51674084), the Fundamental Funds for the central universities (Nos. 150203003, 150202001), the Program of the Natural Science Foundation of Liaoning Province (20170540316), China Postdoctoral Science Foundation (2017M611246), and the NEU Postdoctoral Science Foundation (No. 20160304).

Author Contributions: Songtao Yang and Mi Zhou contributed to the material synthesis, performed the experiments, material characterization, and data analysis, and wrote the paper; Weidong Tang revised the paper and refined the language; Tao Jiang, Xiangxin Xue, and Weijun Zhang contributed to the design of the experiment.

Conflicts of Interest: The authors declare no conflict of interest.

References

1. Zhou, L.H.; Zeng, F.H. Reduction mechanisms of vanadium-titanomagnetite-non-coking coal mixed pellet. *Ironmak. Steelmak.* **2011**, *38*, 59–64.
2. Yang, S.T.; Zhou, M.; Jiang, T.; Wang, Y.J.; Xue, X.X. Effect of basicity on sintering behavior of low-titanium vanadium-titanium magnetite. *Trans. Nonferrous Met. Soc. China* **2015**, *25*, 2087–2094.

3. Zhou, M.; Yang, S.T.; Jiang, T.; Jiang, L.H.; Zhang, J.T.; Xue, X.X. Effects of carbon content on the sintering behavior of low-titanium vanadium-titanium magnetite. *Metall. Res. Technol.* **2016**, *113*, 612–622.
4. Yang, S.T.; Zhou, M.; Tang, W.; Jiang, T.; Xue, X.; Zhang, W. Influence of Coke Ratio on the Sintering Behavior of High-Chromium Vanadium-Titanium Magnetite. *Minerals* **2017**, *7*, 107.
5. Yang, S.T.; Zhou, M.; Jiang, T.; Wang, Y.J.; Xue, X.X. Application of a water cooling treatment and its effect on coal-based reduction of high-chromium vanadium and titanium iron ore. *Int. J. Miner. Metall. Mater.* **2016**, *23*, 1353–1359.
6. Zhou, M.; Jiang, T.; Yang, S.T.; Xue, X.X. Vanadium-titanium magnetite ore blends optimization for sinter strength based on iron ore basic sintering characteristics. *Int. J. Miner. Process.* **2015**, *142*, 125–133.
7. Moskalyk, R.R.; Alfantazi, A.M. Processing of vanadium: A review. *Miner. Eng.* **2003**, *16*, 793–805.
8. Fu, W.G.; Wen, Y.C.; Xie, H.E. Development of intensified technologies of vanadium-bearing titanomagnetite smelting. *J. Iron Steel Res. Int.* **2011**, *18*, 7–10.
9. Fu, W.G.; Xie, H.E. Progress in technologies of vanadium-bearing titanomagnetite smelting in pangang. *Steel Res. Int*. **2011**, *82*, 501–504.
10. Sun, Y.; Lv, Q.; Wang, X.; Zhang, S.; Zhang, J. Computational Insights into Interactions between Ca Species and α-Fe_2O_3(001). *J. Iron Steel Res. Int.* **2014**, *21*, 413–418.
11. Park, H.; Park, J.Y.; Kim, G.H.; Sohn, I. Effect of TiO_2 on the Viscosity and Slag Structure in Blast Furnace Type Slags. *Steel Res. Int.* **2012**, *83*, 150–156.
12. Zhang, G.H.; Kuo-Chih, C.; Mills, K. Modelling Viscosities of CaO–MgO–Al_2O_3–SiO_2 Molten Slags. *ISIJ Int.* **2012**, *52*, 355–362.
13. Choi, J.Y.; Lee, H.G.; Kim, J.S. Dissolution rate of Al_2O_3 into molten CaO-SiO_2-Al_2O_3 slags. *ISIJ Int.* **2007**, *42*, 852–860.
14. Liu, Z.G.; Chu, M.S.; Wanf, H.T.; Zhao, W.; Xue, X.X. Effect of MgO content in sinter on the softening-melting behavior of mixed burden made from chromium-bearing vanadium-titanium magnetite. *Int. J. Miner. Met. Mater.* **2016**, *23*, 25–32.
15. Zhou, M.; Yang, S.T.; Jiang, T.; Xue, X.X. Influence of MgO in form of magnesite on properties and mineralogy of high chromium, vanadium, titanium magnetite sinters. *Ironmak. Steelmak.* **2015**, *42*, 217–224.
16. Papanastassiou, D.; Nicolaou, P.; Send, A. Effect of Al_2O_3 and MgO contents on the properties of the blast furnace slag. *Stahl Undsen* **2000**, *120*, 59–64.
17. Li, Q.; Huang, Z.Z.; Jiang, T.; Yang, Y.B.; Li, G.H. Effect of Dolomite and Serpentine on Sinter Quality and Microstructure. *Iron Steel.* **2006**, *41*, 10–14.
18. Yu, S.R.; Yu, S.J.; Liu, Y.H.; Li, Y.M. Influence of MgO Content on the Sinter Index and the Metallurgical Property. *Angang Technol.* **2008**, *353*, 23–26.
19. Zhou, M.S.; Li, Y.R. Laboratory study on reasonable MgO content in the sinter of Anshan iron and steel group co. *Sinter and Pelletizing.* **2005**, *6*, 1–4.
20. Zhao, Z. Laboratory sinterign study with adding dolomite fines. *Sinter and Pelletizing* **2003**, *28*, 25–27.
21. Yadav, U.S.; Pandey, B.D.; Das, B.K.; Jene, D. Influence of magnesia on sintering characteristics of iron ore. *Ironmak. Steelmak.* **2002**, *29*, 91–95.
22. Yang, L.X.; Davis, L. Assimilation and Mineral Formation during Sintering for Blends Containing Magnetite Concentrate and Hematite/Pisolite Sintering Fines. *ISIJ Int.* **2007**, *39*, 239–245.
23. Zhou, M.; Jiang, T.; Yang, S.T.; Xue, X.X. Influence of basicity on high-chromium vanadium-titanium magnetite sinter properties, productivity, and mineralogy. *JOM-US* **2015**, *67*, 1203–1213.
24. Zhou, M.; Jiang, T.; Yang, S.T.; Xue, X.X. Sintering behaviors and consolidation mechanism of high-chromium vanadium and titanium magnetite fines. *Int. J. Miner. Metall. Mater.* **2015**, *22*, 917–925.
25. Zhou. M. Fundamental Investigation on Cr-bearing Vanadium and Titanium Magnetite Ore in Sintering and Iron-making Process. Ph.D. Thesis, Northeastern University, Shenyang, China, 2015.
26. Tromel, G.; Koch, K.; Fix, W.N. Der Einfluß des Magnesiumoxyds auf die Gleichgewichte im System Fe–CaO–FeO_n–SiO_2 und auf die Schwefelverteilung bei 1600 °C. *Arch. Eisenhuettenwes* **1969**, *40*, 969–978.
27. Knueppel, R.; Helfmeier, H.U.; Oeters, F. Thermodynamic database development modeling and phase diagram calculation in oxide systems. *Arch. Eisenhuettenwes* **1975**, *46*, 549–554.
28. Loo, C.E.; Wan, K.T.; Howes, V.R. Mechanical properties of natural and synthetic mineral phases in sinters having varying reduction degradation indices. *Ironmak. Steelmak.* **1988**, *15*, 279–285.

29. Bristow, N.J.; Loo, C.E. Sintering Properties of Iron Ore Mixes Containing Titanium. *ISIJ Int.* **1992**, *32*, 819–828.
30. Loo, C.E.; Bristow, N.J. Mechanism of low-temperature reduction degradation of iron ore sinters. *Trans. Inst. Min. Metall. Sect. C* **1994**, *103*, 126–135.